



Surface states regulation of sulfide-based photoanode for photoelectrochemical water splitting

Haimei Wang, Yuguo Xia^{*}, Ning Wen, Zhan Shu, Xiuling Jiao, Dairong Chen^{*}

National Engineering Research Center for Colloidal Materials, School of Chemistry & Chemical Engineering, Shandong University, Jinan, Shandong, 250100, China

ARTICLE INFO

Keywords:

CdIn₂S₄
Photoanode
Adaptive junction
Surface states
Photoelectrochemical water splitting

ABSTRACT

Regulating the surface states distribution on the photoanode/electrolyte interface is crucial to photoelectrochemical (PEC) water splitting. Here we develop a CdIn₂S₄/InO_x/NiFe-LDH adaptive junction to improve the PEC performance and stability of bare CdIn₂S₄, which achieves a photocurrent density of 5.47 mA cm⁻² at 1.23 V_{RHE} as well as good durability under AM 1.5G illumination without sacrificial reagent. The experimental characterizations evidence that both the charge carrier density (N_d) and surface states distribution (N_{ss}) alter along with the interfacial structural regulation in the CdIn₂S₄/InO_x/NiFe-LDH photoanode, and a proper ratio of N_{ss}/N_d guarantee the optimal photocurrent. Meanwhile, a strained surface states distribution and negative shifted N_{ss} center facilitate the charge transfer and interfacial water oxidation kinetics as well. This work highlights the influence of interfacial structural regulation on the entangled surface states distribution and charge carrier density and may inspire more excellent work on designing other efficient photoanodes.

1. Introduction

Harvesting sunlight by utilizing the photoelectrochemical (PEC) water splitting strategy to generate clean hydrogen fuel offers a promising route to alleviate the energy and environmental problem [1]. The exquisite selection of electrode materials to achieve an efficient solar-to-hydrogen (STH) conversion is of great importance, especially to the photoanodes in consideration of the sluggish surface water oxidation kinetics [2]. Besides, the light-absorbing semiconductors (sem) integrated with electrocatalysts (cat) to form sem|cat heterojunctions are generally required to address their intrinsic poor photoinduced charge separation and transport properties or improve the electrode/electrolyte interfacial stability [3]. According to the crystallinity of decorated electrocatalysts, the typical sem|cat heterojunctions fall into two categories, that is, buried junction and adaptive junction [4]. Among others, the photovoltage of the adaptive junction depends on the electron quasi-Fermi level under illumination and the surface states distribution on the sem|cat interface [5]. Meanwhile, given the adjustable characteristics of the surface states distribution regulated by experimental conditions, such as applied bias, illumination intensity, electrolyte pH, etc., the photoanodes based on adaptive junctions usually provide larger photovoltages and efficiencies [6–8]. Up to now, photoanodes employing low-density materials as electrocatalysts, such as metal oxides

[9–14] and metal hydroxides [15–17], to construct permeable adaptive junctions have been reported.

The effect of surface states on the PEC performance is not unilateral. Generally, the surfaces states with higher oxidative energy that originated from the adsorbed species are interpreted as surface intermediates involving in the oxygen evolution reaction (OER), while the surface states with lower oxidative energy that related to the surface defects or dangling bonds are assigned to the detrimental recombination center or catalytically inactive sites [18]. Thus, the actual physicochemical processes occurring on the photoanode/electrolyte interface under illumination involve the coupled charge carrier transfer/recombination and OER process. Notably, the charge carrier density and interfacial charge transfer/recombination kinetics are highly dependent on the photoanodes' depletion regions as well [19]. Therefore, regulating the semiconductor's thickness in the adaptive junctions renders the final PEC performance an entangled result between the surface states distribution and charge carrier density. Although some studies concerning surface states influenced by experimental conditions and modified layers have been reported [20–22], the entangled surface states distribution and charge carrier density regulated by the interfacial structure of adaptive junctions are still elusive.

Herein, we construct a CdIn₂S₄/InO_x/NiFe-LDH adaptive junction to improve the PEC performance and interfacial stability of bare CdIn₂S₄

^{*} Corresponding authors.

E-mail addresses: xyg@sdu.edu.cn (Y. Xia), cdr@sdu.edu.cn (D. Chen).

<https://doi.org/10.1016/j.apcatb.2021.120717>

Received 25 July 2021; Received in revised form 4 September 2021; Accepted 10 September 2021

Available online 20 September 2021

0926-3373/© 2021 Elsevier B.V. All rights reserved.

without sacrificial reagent. By precisely regulating the layer thicknesses of CdIn_2S_4 , InO_x , and NiFe-LDH layers, the $\text{CdIn}_2\text{S}_4/\text{InO}_x/\text{NiFe-LDH}$ photoanode reveals superior photocurrent density and stability. Besides, the evolutions of charge carrier density and surface states distribution along with the interfacial structure change are elaborately investigated, which illustrates that a proper ratio of surface states density to charge carrier density accounts for the enhanced photoelectric conversion efficiency. Meanwhile, the effective overlap between the surface states distribution and water density of states guarantees the efficient charge carrier transporting to the interfaces and anticipating the OER processes. This work emphasizes the importance of interfacial structural regulation on the surface states distribution, and demonstrates the entangled effect of surface states density and charge carrier density on the PEC performance.

2. Experimental section

2.1. Electrodeposition of CdIn_2S_4 thin film

Electrodeposition of nanocrystalline CdIn_2S_4 thin film onto FTO glass substrate was carried out on an electrochemical workstation (CHI 760e) at room temperature with a conventional three-electrode cell. The working electrode was FTO glass substrate ($10 \Omega \text{ sq}^{-1}$), the reference electrode was an Ag/AgCl (3 M KCl solution), and a platinum plate was employed as the counter electrode. The FTO glass substrates were ultrasonically pretreated for 30 min successively with acetone, isopropanol, and deionized water and then dried in the N_2 atmosphere at room temperature. The suitable precursor ratio of Cd/In to prepare stoichiometric CdIn_2S_4 was found to be 1:1.5. Therefore, a mixture of 1 mM CdCl_2 , 1.5 mM InCl_3 , and an excess sulfur source (10 mM $\text{Na}_2\text{S}_2\text{O}_3 \cdot 5 \text{H}_2\text{O}$) were prepared with 0.1 M KCl as the supporting electrolyte. Subsequently, the pH of the mixed solution was adjusted to 2–2.5 by adding drops of concentrated 1.0 M HCl in order to decrease the formation of metal complexes such as In(OH)_3 . Finally, the uniform and well-adherent CdIn_2S_4 thin films were deposited at an optimized deposition potential of -1.1 V vs. Ag/AgCl . After each electrodeposition, the obtained CdIn_2S_4 thin films were rinsed with deionized water and then annealed in the sulfur atmosphere at 300°C for 30 min.

2.2. Atomic layer deposition of InO_x film

The InO_x film was deposited on the above-annealed CdIn_2S_4 by the plasma-enhanced ALD method (PEALD-100R, Jiaxing Keming Electronic Equipment Technology Co., Ltd., China). The ALD condition was performed according to ref. [23] with some modifications. The cyclopentadienyl indium (InCp) and oxygen plasma were employed as In oxygen precursors, respectively. Typically, the InCp held in a stainless-steel bubbler was heated to 140°C and delivered to the deposition chamber by an 80 sccm flow of Ar carrier gas. Meanwhile, deionized water and oxygen gas (20 sccm) were used as the co-reactants in the second half-cycle. The temperature for both the chamber's walls and substrate was set at 150°C during the ALD process. The deposition rate was estimated to be 0.1 nm/cycle .

2.3. Electrodeposition of NiFe-LDH layer

The synthesis of NiFe-LDH nanosheets was processed according to ref. [24] with some modification. The solution with stoichiometric molar ratios of Ni^{2+} and Fe^{2+} ions was prepared by dissolving nickel nitrate ($\text{Ni(NO}_3)_2 \cdot 6 \text{H}_2\text{O}$) and iron sulfate ($\text{FeSO}_4 \cdot 7 \text{H}_2\text{O}$) in 100 mL of water under Ar atmosphere to prevent the self-oxidation of Fe^{2+} into Fe^{3+} . The total amount of ions (Ni^{2+} and Fe^{2+}) was kept to 0.15 mol, and the molar ratio of Ni/Fe was 1:1. All the electrochemical depositions were carried out by applying a cathodic potential of -1.0 V vs. Ag/AgCl in the dark.

2.4. Characterizations

The crystalline structures were analyzed by pXRD (D8, Bruker AXS) with $\text{Cu K}\alpha$ radiation ($\lambda = 1.5418 \text{ \AA}$). The morphology and microstructure were characterized using SEM (Hitachi, SU8010) and high-resolution TEM (JEM-1011, JEOL). The XPS (EscaLab 250Xi, Thermo scientific) technique with 30.0 eV pass energy and an $\text{Al K}\alpha$ line excitation source was employed to identify the elemental compositions and bonding information. The binding energy reference was taken at 284.8 eV for the C 1s peak arising from surface hydrocarbons. The optical absorption properties were studied using UV–visible diffuse reflectance spectra (Cary 100, Agilent Technologies). The photoluminescence spectra (P.L., G9800A, Agilent Technologies) were measured with an excitation wavelength at 370 nm in the range of 420 and 650 nm.

2.5. PEC property measurements

The PEC performance of these photoanodes was performed on an electrochemical workstation (CHI 760e) at room temperature with a conventional three-electrode cell. The saturated Ag/AgCl electrode, Pt electrode, and as-prepared photoanode with an exposed area of $1 \times 1 \text{ cm}^2$ are separately employed as the reference electrode, counter electrode, and working electrode. A 300 W Xe arc lamp (CEL-PE300L-3A, Cealight Technology Co. Ltd., China) with an AM 1.5G filter was employed to simulate solar illumination with about 1 Sun power. The back-side illumination through the FTO side was adopted for all the PEC tests under 1 M KOH electrolyte without any sacrificial reagent. The gas evolution was analyzed by gas chromatography (3420A, Beifen-Ruili0020 Co. Ltd., China) with a three-electrode system at 1.2 V vs. RHE.

Supplementary equations to evaluate charge separation (η_{se}) and injection (η_{in}) efficiencies [25]:

$$J_{\text{ph}} = J_{\text{abs}} \times \eta_{\text{se}} \times \eta_{\text{in}} \quad (1)$$

$$J_{\text{abs}} = \frac{q}{hc} \int \lambda \phi_{\lambda} \eta_{\text{abs}} d\lambda \quad (2)$$

$$\eta_{\text{se}} = J_{\text{ph}}^{N_{\text{a}_2\text{S}_3\text{O}_3}} / J_{\text{abs}} \quad (3)$$

$$\eta_{\text{in}} = J_{\text{ph}}^{H_2O} / J_{\text{ph}}^{N_{\text{a}_2\text{S}_3\text{O}_3}} \quad (4)$$

$$\eta_{\text{abs}} = (1 - 10^{-A}) \times 100\% \quad (5)$$

The $J_{\text{ph}}^{N_{\text{a}_2\text{S}_3\text{O}_3}}$ was the photocurrent density measured in 1 M KOH and 0.5 M $\text{Na}_2\text{S}_3\text{O}_3$ mixed electrolyte, which served as hole scavengers to ensure the hole injection rate approaching 100%, and $J_{\text{ph}}^{H_2O}$ was the photocurrent densities measured in 1 M KOH. The J_{abs} was the photon adsorption rate expressed as the photocurrent density, and the q was the charge of an electron, h was the Plank constant, c was the light speed, ϕ_{λ} was the photon flux of the AM 1.5G solar spectrum, and η_{abs} was the light absorption efficiency.

2.6. Measurement of Mott–Schottky plots

The Mott–Schottky spectra were obtained in the voltage window of -1.5 – 0 V vs. Ag/AgCl in the dark with the frequency of 1 kHz. The charge carrier density in the space charge region was calculated according to the Mott–Schottky equation:

$$\frac{1}{C^2} = \frac{2}{\epsilon \epsilon_0 A^2 q N_d} \times \left(V - V_{\text{fb}} - \frac{k_B T}{q} \right) \quad (6)$$

Where C was the space-charge capacitance, V (V vs. RHE) was the applied voltage, V_{fb} (V vs. RHE) was the flat-band potential, N_d was the charge carrier density, ϵ was the dielectric constant of the

semiconductor (taken as 6.6 for the CdIn_2S_4 [26]), ϵ_0 was the vacuum permittivity, k_B was the Boltzmann constant, q was the electronic charge, and T was the absolute temperature.

The thickness of the depletion width (W_d) could be calculated as [27]:

$$W_d = \left[\frac{2\epsilon_0\epsilon(V - V_{fb})}{qN_d} \right]^{1/2} \quad (7)$$

2.7. IMPS and PEIS measurements

The IMPS and PEIS measurements were carried out using a potentiostat (Zahner PP211, Zahner, German) in the 1 M KOH solution with a three-electrode configuration at different bias potentials. The high-intensity light-emitting diode (LED: LSW-2) source was employed as the light source for the controlled IMPS and PEIS tests. The wavelength of light was 430–720 nm in the visible light region with an average intensity of 100 mW cm^{-2} . The small ac perturbation of light was set to 10% of the dc bias light during IMPS tests. IMPS tests were performed with the frequency range from 10 kHz to 100 MHz, and PEIS tests were performed with the frequency range from 100 kHz and 100 MHz under illumination. Moreover, The Randles equivalent circuit was used to analyze the impedance data using the Zview software (Scribner Associates).

In a typical IMPS response, the frequency at the maximum imaginary part corresponded to the sum of the charge transfer (k_{tran}) and recombination (k_{rec}) rate constants as expressed [28],

$$k_{\text{tran}} + k_{\text{rec}} = 2\pi f_{\text{max}} \quad (8)$$

Besides, the hole transfer efficiency (η_{tran}) at the semiconductor/electrolyte interface could be determined by the ratio of the steady-state photocurrent (j_{ss}) to the instantaneous photocurrent (j_{hole}). Assuming that both hole transfer and recombination were pseudo-first-order in the surface hole concentration, the hole transfer efficiency could also be expressed by the ratio of k_{rec} and k_{tran} ,

$$\eta_{\text{tran}} = \frac{j_{\text{ss}}}{j_{\text{hole}}} = \frac{k_{\text{tran}}}{k_{\text{tran}} + k_{\text{rec}}} \quad (9)$$

The average photogenerated electron transfer time (τ_d) could be estimated from the frequency at the minimum imaginary part,

$$\tau_d = \frac{1}{2\pi f_{\text{min}}} \quad (10)$$

2.8. Theoretical calculations

DFT calculations corrected by on-site Coulomb interaction and dispersion interactions (DFT-D3) were performed with the projected augmented wave method, as implemented in the Vienna Ab-initio Simulation Package [29,30]. The exchange-correction function was treated by the generalized gradient approximation (GGA) of Perdew–Burke–Ernzerhof functional, and the wave functions were expanded on a plane wave basis with an energy cutoff of 500 eV. The effective U – J values, which were applied to the d -orbitals of Ni and Fe atoms, were taken as 5.20 and 2.56 eV, respectively.[31] The dispersion interactions involved in the $\text{CIS}/\text{InO}_x/\text{NiFe-LDH}$ heterojunction model were corrected by the van der Waals functionals (optPBE) [31]. The gamma-centered scheme for K-points grid sampling was applied for all the calculations. For all the calculations, the convergence criteria for the electronic and ionic relaxations are 10^{-5} eV and 0.02 eV/\AA , respectively.

3. Results and discussion

3.1. Synthesis and characterizations of $\text{CIS}/\text{InO}_x/\text{NiFe-LDH}$ photoanode

Fig. 1a displays the synthesis procedures for $\text{CIS}/\text{InO}_x/\text{NiFe-LDH}$ photoanode, which involve three steps, i.e., electrodeposition for CIS layer, plasma-enhanced atomic layer deposition (PEALD) for InO_x layer, and electrodeposition for NiFe-LDH layer (experimental details are supplemented in experimental section). The powder X-ray diffraction (pXRD) patterns of as-synthesized samples are firstly characterized (Fig. 1b), which reveals that only characteristic peaks of FTO and cubic CdIn_2S_4 (CIS, JCPDS no.27-0060) are observed, indicative of the low crystallinities of InO_x and NiFe-LDH layers. The morphology evolutions along with the synthesis procedures are further investigated by scanning electron microscopy (SEM). As depicted in Fig. 1c–f, the CIS nanospheres constructed by primary particles of $<100 \text{ nm}$ are generated; meanwhile, the InO_x layer does not change the sphere-like morphology, and the NiFe-LDH nanosheets vertically grow on the InO_x layer. The spatial elemental distributions in $\text{CIS}/\text{InO}_x/\text{NiFe-LDH}$ hybrid are measured by high-angle annular dark-field scanning transmission electron microscopy (HAADF-STEM) equipped with energy dispersive X-ray mapping (Fig. 1g), in which the signals of Cd, In, and S (Fe and Ni) mainly concentrate on the interior zone (outer shell), illustrative of the successful synthesis of the $\text{CIS}/\text{InO}_x/\text{NiFe-LDH}$ hybrid hierarchical superstructure. The high-resolution TEM (HR-TEM) image confirms that the lattice spacing of the InO_x layer corresponds to the (400) crystal plane of cubic In_2O_3 (JCPDS no. 06-0416), which epitaxially grows along [010] direction of CIS in consideration of its lattice parameter matching with (400) crystal plane of CIS (Fig. 1h). To elucidate the possible electronic structural changes in $\text{CIS}/\text{InO}_x/\text{NiFe-LDH}$ hybrid, we performed density functional theory (DFT) calculations corrected by on-site Coulomb interaction (DFT+ U) and dispersion interaction (optPBE, van der Waals functionals) (Fig. S1, simulation details are supplemented in computational section). Compared with the density of states (DOS) of bare CIS, midgap states mainly consisted of Ni 3d and O 2p orbitals generate in $\text{CIS}/\text{InO}_x/\text{NiFe-LDH}$ hybrid (Fig. 1i), which stretches over the Fermi level, indicative of its largely improved conductivity. Meanwhile, the midgap states may reveal strong Urbach tail absorption and serve as separation centers for photoinduced carriers, resulting in enhanced light absorption and charge separation. More importantly, the frontier orbitals, especially for those involved in the valence band, have been converted from S 2p orbitals in CIS to Ni 3d orbitals in $\text{CIS}/\text{InO}_x/\text{NiFe-LDH}$ hybrid, which could prevent the photooxidation process of CIS and increases the stability of $\text{CIS}/\text{InO}_x/\text{NiFe-LDH}$ photoanode [32, 33].

3.2. Optical and photoelectrochemical characterizations

The photoelectric conversion efficiency of a photoanode is theoretically positively correlated with photon absorption rate (J_{abs}), charge separation efficiency (η_{se}), and injection efficiency (η_{in}) (Eq. 1) [34]. Thereby, to illustrate the effect of InO_x and NiFe-LDH layers and subsequently confirm their main contributions, we further measure the optical and photoelectrochemical properties. In advance of calculating the above parameters, the possible charge transfer and energy band structures in $\text{CIS}/\text{InO}_x/\text{NiFe-LDH}$ are rationally estimated. We firstly conduct the X-ray photoelectron spectroscopy (XPS) measurement to investigate the surface elemental charge state evolution along with InO_x and NiFe-LDH modification. The downshifts of Cd 4d orbitals confirm the interfacial charge transfer from bare CIS to NiFe-LDH layer under dark, indicative of the internal built field towards the external surface and beneficial to the photoinduced electrons transporting to the internal circuit (Fig. S2). The exact energy band structures for bare CIS and NiFe-LDH are further determined by ultraviolet photoelectron spectroscopy (UPS, Fig. S2), which reveals a band-matching structure between CIS and NiFe-LDH. In addition, the InO_x layer is supposed to

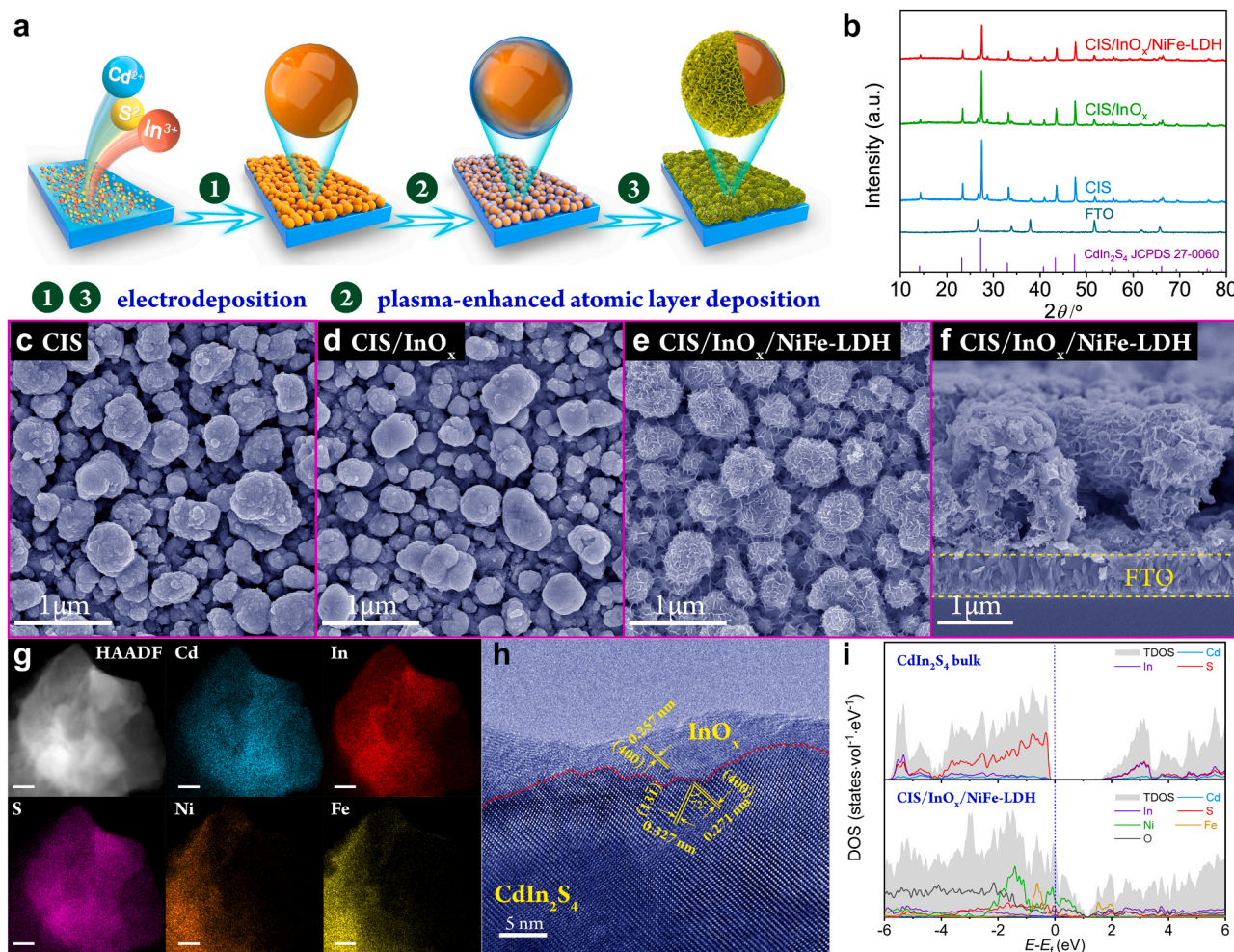


Fig. 1. (a) The schematic diagram for the synthetic protocol of CIS/InO_x/NiFe-LDH photoanode. (b) pXRD patterns. (c-e) The SEM images for CIS, CIS/InO_x, and CIS/InO_x/NiFe-LDH, respectively. (f) The typical cross-section SEM image of CIS/InO_x/NiFe-LDH. (g) The HAADF-STEM energy dispersive X-ray mapping. The bars represent 10 nm. (h) The HR-TEM image for CIS/InO_x. (i) The density of states for CdIn₂S₄ bulk and CIS/InO_x/NiFe-LDH heterojunction.

transfer photoinduced holes based on the quantum tunneling effect as other metal oxides [35–37]. Thereby, the CIS/InO_x/NiFe-LDH photoanode should possess enhanced photoinduced charge separation and injection efficiencies.

No distinct absorbance edge shifts are observed in the UV–vis diffuse reflection spectra (DRS, Fig. 2a) for CIS with InO_x and NiFe-LDH modification. Meanwhile, the J_{abs} values derived from the DRS spectra also reveal little improvement for CIS/InO_x/NiFe-LDH ranging from 300 nm to 800 nm (Fig. 2b, Eq. 2), indicative that the photon absorption rate does not dominate in PEC performance. Conversely, the η_{se} and η_{in} values are significantly increased (Fig. 2c and d, Eqs. 3 and 4), suggesting that the InO_x and NiFe-LDH layers mainly contribute to the charge separation and charge injection processes, consistent with the above speculation. Moreover, the time-resolved transient photoluminescence (TRPL) spectra are recorded to probe the specific charge carrier dynamics in as-synthesized photoanodes (Fig. 2e). The PL decay curves can be well fitted to a triexponential model, and the CIS/InO_x/NiFe-LDH photoanode manifests the longest average lifetime, indicating that more photoinduced electrons and holes can participate in the PEC process. Meanwhile, the steady-state photoluminescence (PL) spectra (Fig. 2f) also confirm the decreased recombination rate for the photoinduced electron-hole pair, indicative of more efficient charge separation and transfer in the CIS/InO_x/NiFe-LDH photoanode. Briefly, the fundamental optical and photoelectrochemical characterizations illustrate that the charge separation and charge injection rather than optical

absorption are greatly enhanced in CIS/InO_x/NiFe-LDH photoanode, indicative of an improved PEC performance.

3.3. PEC performance of the CIS/InO_x/NiFe-LDH photoanode

The PEC performance of CIS/InO_x/NiFe-LDH photoanode was investigated with a conventional three-electrode cell. Given the significant impact of interface structures on the PEC properties, the layer thicknesses of CIS, InO_x, and NiFe-LDH are optimized in advance (Fig. S3). Besides, the bare CIS and CIS/NiFe-LDH photoanodes are also prepared to serve as contrasts to illustrate the inherent mechanism for the enhanced PEC performance. Due to the nearly unchanged J - V plot of CIS/InO_x compared to bare CIS and its instability in the alkaline electrolyte (Fig. S4), which illustrates the surface of CIS photoanode solely modified with InO_x layer can not promote the PEC performance. Thereby, the influence of the InO_x layer on the PEC performance is elaborated by comparing the data discrepancy between CIS/NiFe-LDH and CIS/InO_x/NiFe-LDH photoanodes. The J - V plots display the largely enhanced photocurrent density in CIS/InO_x/NiFe-LDH photoanode (Fig. 3a), achieving a value of 5.47 mA cm⁻² at 1.23 V_{RHE} in 1 M KOH electrolyte under AM 1.5 G illumination, which is comparable to other up-to-date promising photoanodes (Table S1). Besides, the cathodic shift of the onset potential (E_{on}) in CIS/InO_x/NiFe-LDH photoanode suggests its improved OER kinetics with InO_x and NiFe-LDH modification (Fig. S5) [38]. The open-circuit voltages are also

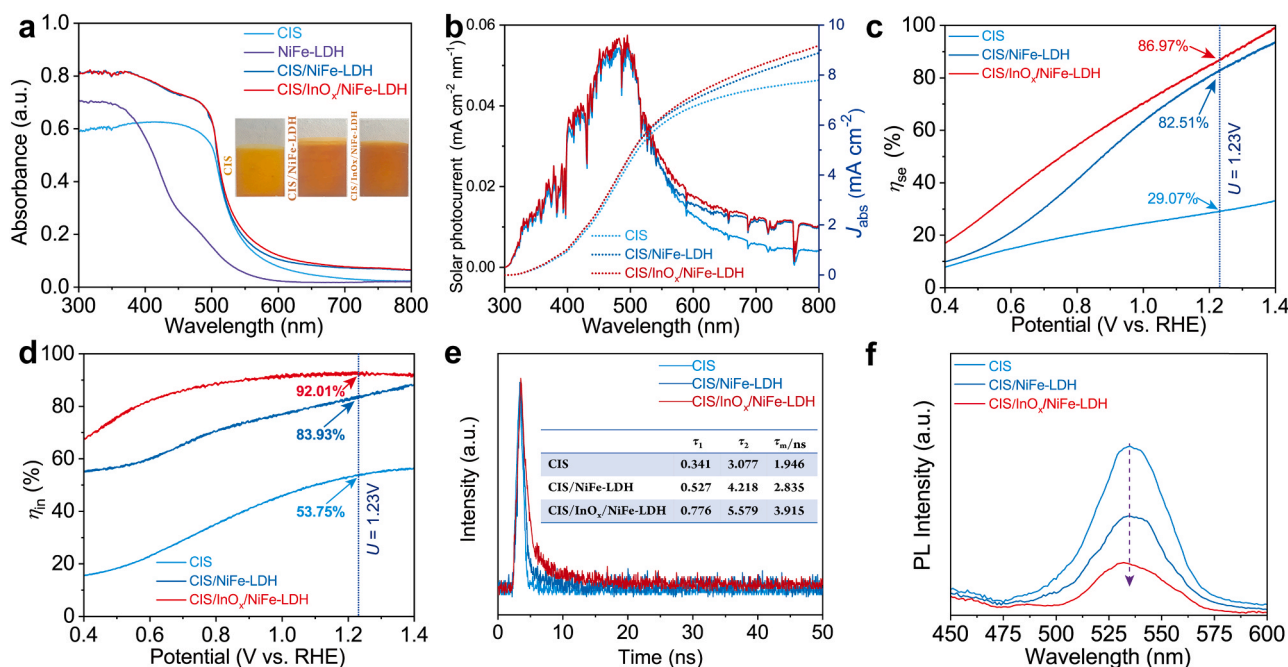


Fig. 2. (a) UV-vis diffuse reflectance spectra. Insets correspond to their optical images. (b) The solar photocurrents and corresponding photon absorption rates (J_{abs}) of the as-synthesized photoanodes. (c) Charge separation efficiency related to the photoinduced electron-hole separation process vs. potential curves. (d) Charge injection efficiency associated with the photoinduced hole transfer to the photoanode/electrolyte interfaces. (e) Time-resolved transient PL decay spectra with excitation wavelength $\lambda_{\text{ex}} = 370$ nm. Inset is the fitted results based on a triexponential model $I(t) = \sum_{i=1}^3 A_i e^{-t/\tau_i}$, where $I(t)$, τ_i , and A_i were the intensity, lifetime, and amplitude of the i_{th} component, respectively. (f) Steady-state PL spectra.

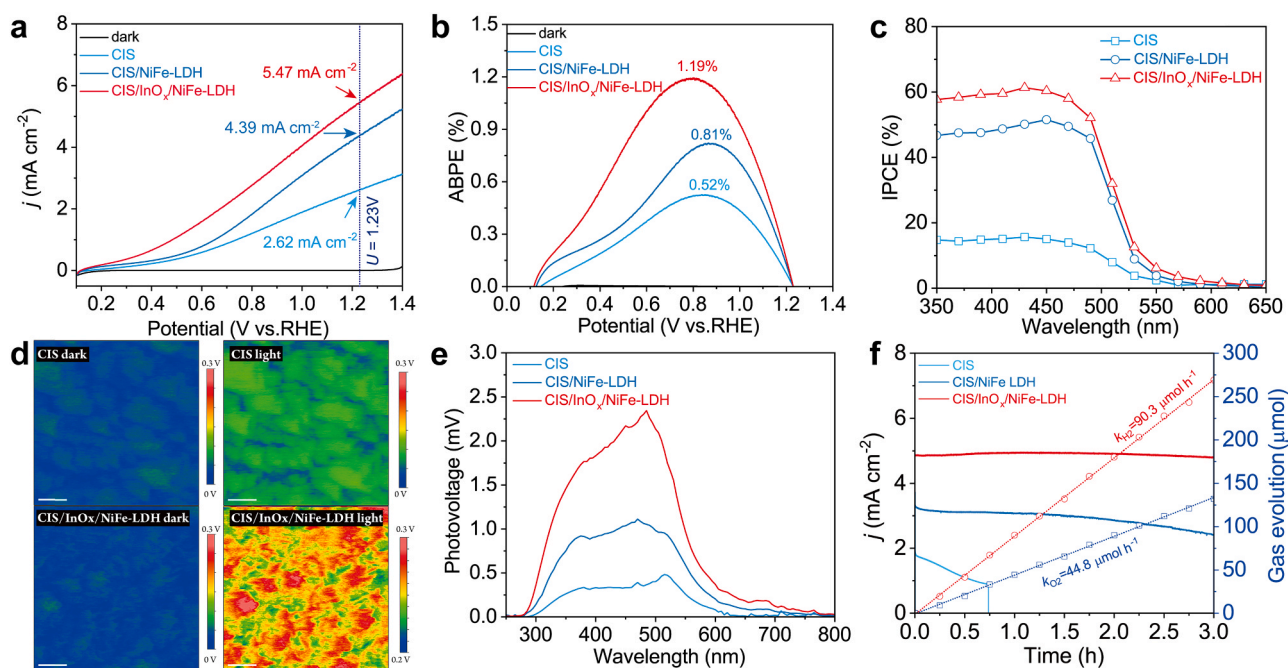


Fig. 3. (a) Current-voltage (J - V) plots measured in 1 M KOH under dark and AM 1.5G (100 mW cm^{-2}) illumination with a scan rate of 10 mV s^{-1} . (b) ABPE measured with a two-electrode cell for water splitting under dark and illumination. (c) IPCE measured at $0.6 \text{ V}_{\text{RHE}}$ under monochromatic light irradiation. (d) V_{CPD} mapping of CIS and CIS/InO_x/NiFe-LDH surfaces under blue light irradiation ($\lambda = 450$ nm). (e) SPV spectra. (f) Long-term stability, and experimental and theoretical H_2 evolution, are measured under AM 1.5 G illumination.

measured (Fig. S6), and the CIS/InO_x/NiFe-LDH photoanode reveals the highest photovoltage value (V_{ph}), suggesting its best photon-to-current conversion efficiency. The photoelectrochemical performance is thereby evaluated by applied bias solar energy conversion efficiencies (ABPE). The CIS/InO_x/NiFe-LDH photoanode achieves a maximum

ABPE value of 1.19% at $0.795 \text{ V}_{\text{RHE}}$ and two-fold that of bare CIS photoanode (Fig. 3b, Table S1). Meanwhile, the incident photon-to-current conversion efficiencies (IPCE) under monochromatic light irradiation are further calculated to illustrate the changes in photoresponse. As depicted in Fig. 3c, the IPCE value of CIS/InO_x/NiFe-LDH photoanode is

significantly improved, especially in the light range of 350–500 nm. To understand the inherent reason for the enhanced IPCE value in CIS/ InO_x /NiFe-LDH photoanode, we further calculate the absorbed photon-to-current efficiency (APCE) to eliminate the influence of the photon absorption rate (Fig. S7). The APCE values reveal a consistent tendency as in the ABPE, indicative of the decisive factors of InO_x and NiFe-LDH layers in charge separation and injection, which is also consistent with the above photoelectric conversion efficiency measurements.

Besides, Kelvin probe force microscopy (KPFM) is utilized to directly illustrate the charge separation and transport through the contact potential difference (V_{CPD}) between the photoanode's surface and Pt/Ir coated tip that grounded to the Au film. The topographic AFM images and V_{CPD} mapping for bare CIS and CIS/ InO_x /NiFe-LDH are shown in Fig. S8 and Fig. 3d. The positive values of V_{CPD} illustrate the hole density accumulation on the photoanodes under blue light irradiation, and the significantly increased V_{CPD} in CIS/ InO_x /NiFe-LDH photoanode evidence the enhanced charge separation and charge injection with InO_x and NiFe-LDH modification [39]. To further unravel the effect of InO_x and NiFe-LDH layers on the electron-hole separation efficiency in CIS/ InO_x /NiFe-LDH photoanode, the surface photovoltage (SPV)

spectroscopy is measured as well (Fig. 3e). The positive photovoltage values indicate the transition route, that is, the transport of photoinduced electrons via the surface states of photoanodes to the conduction band [40]. By contrast, the increased photovoltages in CIS/ InO_x /NiFe-LDH photoanode indicate the synergistic effect of InO_x and NiFe-LDH layers. The PEC stability and hydrogen evolution of the CIS/ InO_x /NiFe-LDH photoanode are investigated by the long-term photocurrent to time (J - t) measurement at 1.2 V_{RHE} and gas chromatography, respectively (The schematic diagram and video for the long-term PEC test are revealed in Fig. S9 and supplementary video). No evident decay is observed for CIS/ InO_x /NiFe-LDH photoanode after 3 h continued operation in 1 M KOH electrolyte, illustrative of the stable characteristic of CIS/ InO_x /NiFe-LDH hybrid photoanode (Fig. 3f). Besides, no noticeable phase structural, morphological, and electronic structural changes are observed in the post-PEC measured CIS/ InO_x /NiFe-LDH photoanode (Fig. S10), further evidencing its good stability. Meanwhile, the CIS/ InO_x /NiFe-LDH photoanode achieves a hydrogen evolution rate of 90.3 $\mu\text{mol h}^{-1} \text{cm}^{-2}$, approaching its theoretical value as denoted by the dashed line, also illustrative of ca. 100% Faradaic efficiency for hydrogen evolution (Fig. S11).

Supplementary material related to this article can be found online at

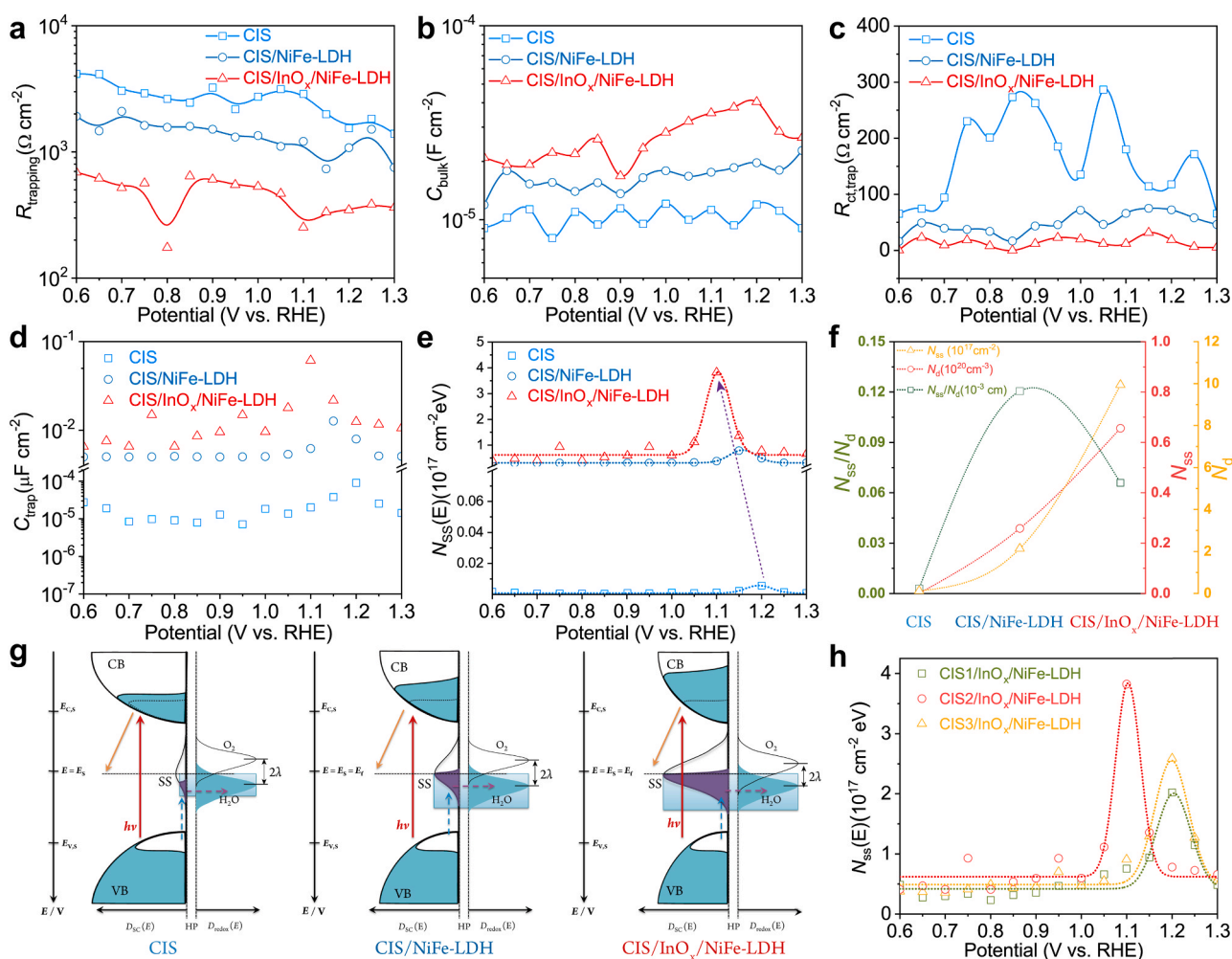


Fig. 4. Capacitances and resistances parameters associated with the (a–b) charge trapping (R_{trapping} , C_{bulk}) and (c–d) transfer (R_{ct} , R_{trap} , C_{trap}) at/from surface states with different applied potentials that are determined from the PEIS spectra. (e) DOS of surface states of CIS, CIS/NiFe-LDH, and CIS/ InO_x /NiFe-LDH photoanodes as a function of applied potentials derived from the C_{trap} . The lines are fitted by a Gaussian model. (f) Surface states density (N_{ss}), charge donor density (N_{d}), and their ratio ($N_{\text{ss}}/N_{\text{d}}$) of CIS, CIS/NiFe-LDH, and CIS/ InO_x /NiFe-LDH photoanodes. The N_{ss} value was obtained from the integration of fitted DOS profiles, and N_{d} was derived from the Mott-Schottky plots. (g) The schematic diagram of the surface states distribution for the photoanode/electrolyte interface under illumination with 1.23 V_{RHE} applied bias. λ represents the redox coupled reorganization energy [20]. (h) DOS of surface states for CIS/ InO_x /NiFe-LDH adaptive junction with different layer thicknesses of CIS layer. The CIS layer's thickness is regulated through electrodeposition time, where CISx ($x = 1, 2, 3$) represents the electrodeposition time for 60, 120, and 180 s, respectively.

doi:10.1016/j.apcatb.2021.120717.

3.4. Surface states regulation of the CIS/InO_x/NiFe-LDH photoanode

Given the key determinants of surface states in the observed PEC performance, regulating surface states to achieve enhanced OER kinetics and suppressed photoinduced charge carriers recombination is of great necessity [3]. Here we employed photoelectrochemical impedance spectroscopy (PEIS) to illustrate the surface state redistribution in CIS photoanode with InO_x and NiFe-LDH modification. The charge trapping (R_{trapping} , C_{bulk}) and transfer ($R_{\text{ct, trap}}$, C_{trap}) values derived from the PEIS results are plotted according to the corresponding equivalent circuit (Fig. S12). According to the definitions of these physical quantities in the fitted model [41], the decreased R_{trapping} value in CIS/InO_x/NiFe-LDH illustrates the restrained recombination of trapping electrons and holes (Fig. 4a), while the enhanced C_{bulk} value indicates the increased carrier density after CIS photoanode with InO_x and NiFe-LDH modification (Fig. 4b). Thereby, the charge carrier density (N_d) derived from the Mott-Schottky measurement (Eq. 6) is quantitatively calculated (Fig. S13). The N_d value of CIS/InO_x/NiFe-LDH photoanode is estimated to be $9.94 \times 10^{20} \text{ cm}^{-3}$, revealing tremendous improvement compared to that of bare CIS photoanode ($1.12 \times 10^{19} \text{ cm}^{-3}$). Besides, the strong correlation between the decreased $R_{\text{ct, trap}}$ and increased C_{trap} in CIS/InO_x/NiFe-LDH evidences the accumulation of holes in surface states at the photoanode/electrolyte interface (Fig. 4c and d) [42]. Despite the C_{bulk} and C_{trap} revealing similar tendencies along with applied potentials, the more dramatic changes and relatively larger values in C_{trap} also illustrate that most of the photoinduced charges mainly locate on the surface states.

To highlight the role of the surface states in the charge transfer process, we calculate the energetic distribution of density of states (DOS) by $N_{\text{ss}}(E) = C_{\text{trap}}(E)/q$ (Fig. 4e) [43], where $N_{\text{ss}}(E)$ is the DOS of the surface states as a function of potential, and q is the elementary charge. The N_{ss} distributions display Gaussian behavior, and notably, only the surface states with higher oxidative energy that interpreted as the reaction intermediate are observed for all the photoanodes, suggesting that few defects are generated at the surface of bare CIS, and the detrimental surface states that acting as recombination centers are eliminated by the NiFe-LDH layer. Besides, except for the significantly increased DOS, the left shift of N_{ss} center in CIS/InO_x/NiFe-LDH also indicates a decrease in the backward rate constant for the intermediate steps in the OER which is favorable to the surface water oxidation reaction [44]. To quantitatively analyze the effect of N_{ss} and N_d in photocurrent, we summarize the values of N_{ss} , N_d , and the N_{ss}/N_d ratio (Fig. 4f). There is neither enough N_d to guarantee a good conductivity or enough N_{ss} to provide reactive sites in bare CIS, which is responsible for its larger $R_{\text{ct, trap}}$ and smaller C_{bulk} values. Meanwhile, despite the largely increased N_{ss} to ensure a fast surface water oxidation reaction in CIS/NiFe-LDH, the relatively insufficient N_d restricts its overall photocurrent. Therefore, the enhanced photocurrent in CIS/InO_x/NiFe-LDH photoanode must be a balanced result between N_d and N_{ss} , and the optimal ratio of N_{ss}/N_d for CIS/InO_x/NiFe-LDH is determined to be $3.15 \times 10^{-5} \text{ cm}$. Besides, the depletion width (W_d) is dependent on the charge donor density (Eq. 7) [45], which dramatically suppressed from 7.32 to 0.89 nm upon InO_x and NiFe-LDH modification, indicative of the enhanced band bending for hole collection, resulting in the acceleration of hole drift from the depletion region to the surface and the suppression of the charge recombination in CIS/InO_x/NiFe-LDH photoanode [46]. The negative shift of flat band potential (V_{FB}) also indicates a sharper band bending in the CIS/InO_x/NiFe-LDH photoanode [47]. Accordingly, the schematic diagrams to illustrate the charge generation and transfer process at the photoanode/electrolyte have been plotted (Fig. 4g). The maximum overlap between the surface states distribution and water density of states guarantees the most efficient charge carrier transfer in CIS/InO_x/NiFe-LDH photoanode. To further verify the entangle effect of N_d and N_{ss} in the surface states regulation, we additionally prepared

CIS/InO_x/NiFe-LDH photoanode with different thicknesses of the CIS layer given its adaptive junction characteristic. Either increasing or decreasing the CIS layer's thickness in CIS/InO_x/NiFe-LDH photoanode brings about the decline of the photocurrent (Fig. S14). Moreover, the N_{ss}/N_d ratios in CIS1/InO_x/NiFe-LDH and CIS3/InO_x/NiFe-LDH photoanodes fluctuate above or below the optimal value (Fig. S15). Meanwhile, the inferior CIS layer's thicknesses also cause positive shifts of N_{ss} centers, resulting in the increase of the adverse OER backward rates (Fig. 4h). Thus, regulating the surface states distribution to achieve an optimal N_d and N_{ss} equilibrium is vital to achieving improved photocurrent.

3.5. Charge transfer/recombination dynamics and OER mechanism

The behavior of photoinduced charge carriers across the Helmholtz layer is further explored to unveil the charge transfer and recombination kinetics involved in the CIS/InO_x/NiFe-LDH photoanode. We employ intensity-modulated photocurrent spectroscopy (IMPS) to evaluate the pseudo-first-order rate constants of surface recombination (k_{rec}) and hole transfer (k_{tran}) [48]. Fig. 5a manifests the typical IMPS responses of CIS, CIS/NiFe-LDH, and CIS/InO_x/NiFe-LDH photoanodes in the complex plane, where the upper quadrant semicircle (charge transport and relaxation inside the photoanode) and lower quadrant semicircle (competition between interfacial charge transfer and recombination) vary a lot [49]. The values of k_{rec} and k_{tran} can be deduced from IMPS spectra measured at different applied biases (Fig. S16, Eqs. 8 and 9). The decreased k_{rec} value and increased k_{tran} value in CIS/InO_x/NiFe-LDH photoanode illustrate the improved charge separation/transfer dynamics (Fig. 5b and c). Specifically, the k_{tran} value does not reveal much increase in CIS/NiFe-LDH photoanode, indicating that the InO_x layer mainly contributes to the charge transfer process in CIS/InO_x/NiFe-LDH photoanode. The average photoinduced electron transfer time (τ_d) estimated from the frequency at the lowest imaginary part (Eq. 10) reveals a much shorter value (Fig. 5d), again illustrating the superior charge transfer dynamics in CIS/InO_x/NiFe-LDH photoanode.

Except for the enhanced charge transfer and suppressed recombination dynamics in the CIS/InO_x/NiFe-LDH photoanode, both the increased charge injection efficiency and oxygen release rate indicate the improved water oxidation kinetics. To assess the activation energy (E_a) of the surface oxygen evolution reaction, which can be extracted from the slope of the Arrhenius plot [50], we measured the variation of current density along with the temperature. As revealed in Fig. 5e, the CIS/InO_x/NiFe-LDH photoanode exhibits the minimum E_a value of 4.8 kJ mol^{-1} , which is significantly lower than those of bare CIS photoanode (10.6 kJ mol^{-1}) and CIS/NiFe-LDH (15.0 kJ mol^{-1}), also indicative of the synergistic effect of the InO_x and NiFe-LDH layers in accelerating the surface OER kinetics. Moreover, to eliminate the discrepancy of interfacial OER kinetics caused by the modified electrocatalysts, the E_a values of CISx/InO_x/NiFe-LDH are simultaneously measured. The CISx/InO_x/NiFe-LDH photoanodes display little changes in E_a values (Fig. S17), indicating a similar OER evolution mechanism. However, the much smaller Tafel slope of CIS2/InO_x/NiFe-LDH illustrates the effect of surface state density on the coupled OER process (Fig. S18); that is, the optimal surface states distribution and negative shifted N_{ss} center facilitate the charge transfer and interfacial water oxidation kinetics. To further elucidate the potential-determining step in the water oxidation process, we additionally calculated the Gibbs free energy evolution of the involved crucial intermediates (*OH, *O, and *OOH). Notably, apart from the decreased largest Gibbs free energy difference in CIS/InO_x/NiFe-LDH hybrid ($\Delta G = 1.852 \text{ eV}$) compared to bare CIS ($\Delta G = 2.418 \text{ eV}$), the rate-determining step (RDS) has been changed from the *OOH formation process to the *O formation process (Fig. 5f-g). Meanwhile, the decreased Gibbs free energy in CIS/InO_x/NiFe-LDH hybrid corresponds to the reduced overpotential ($\eta_{\text{OER}} = 0.622 \text{ V}$), which is also the fundamental reason for the reduced E_a value in CIS/InO_x/NiFe-LDH photoanode. The experimental J - V plots

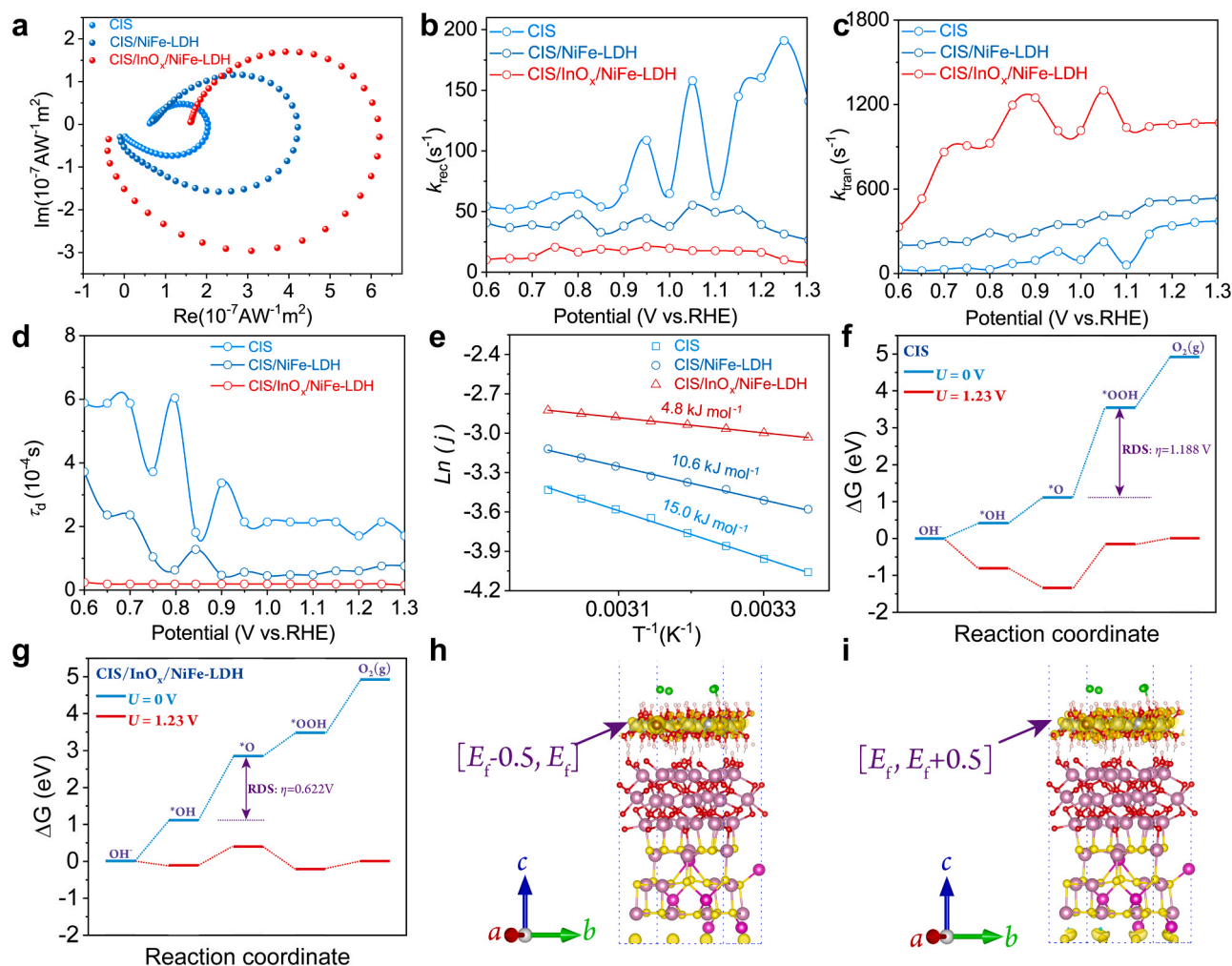


Fig. 5. (a) IMPS spectra of the CIS, CIS/NiFe-LDH, and CIS/InO_x/NiFe-LDH photoanodes under the applied bias of 1.2 V. (b) The plot of the rate constant of charge recombination vs. potential. (c) The plot of the rate constant charge transfer rate vs. potential. (d) The plot of the average lifetime of photoinduced electrons (τ_d) vs. potential. (e) Arrhenius plot of the kinetic current at $\eta = 200$ mV without light illumination. (f) Free energies evolution of OER steps for CdIn₂S₄. (g) Free energies evolution of OER steps for CIS/InO_x/NiFe-LDH heterojunction. Photoexcited charge-transition routes for CIS/InO_x/NiFe-LDH from the (h) HOMO states (in the range of 0–0.5 eV below the Fermi level) to the (i) LUMO states (in the range of 0–0.5 eV above the Fermi level) with an applied bias of 1.23 V. The yellow regions represent the charge accumulation and the isosurface set at $0.01e$ Bohr⁻³.

and Tafel slopes without illumination also confirm the reduced overpotential and improved kinetics in CIS/InO_x/NiFe-LDH photoanode (Fig. S19), consistent with the above theoretical results. Moreover, to unravel the possible photoexcited charge-transfer route under applied bias, the charge density transition from the hybrid highest occupied molecular orbital (HOMO) states to the lowest unoccupied molecular orbital (LUMO) states of CIS/InO_x/NiFe-LDH heterojunction are plotted (Fig. 5h and i). Compared to the bare CIS (Fig. S20), the photoexcited charges in both the HOMO and LUMO states of CIS/InO_x/NiFe-LDH heterojunction concentrate upon the NiFe-LDH layer rather than CIS, which is considered to be responsible for its improved PEC stability.

4. Conclusions

In summary, we prepared a CIS/InO_x/NiFe-LDH adaptive junction to improve the PEC performance of bare CIS and prevent its photooxidation without sacrificial reagent. The photoelectrochemical characterizations illustrate that the InO_x and NiFe-LDH layers mainly contribute to the charge separation and injection processes. The DFT calculations confirm the decreased Gibbs free energy for the rate-determining step with InO_x and NiFe-LDH modification, responsible for the enhanced water oxidation kinetics. Besides, the evolutions of the entangled charge

carrier density and surface states distribution along with the interfacial structural changes are investigated in detail. A proper N_{ss}/N_d ratio guarantees an effective overlap between the surface state distribution and water density states. Meanwhile, a strained surface states distribution and negative shifted N_{ss} center facilitate the charge transfer and interfacial water oxidation kinetics as well. Benefit from the constructed adaptive junction, the CIS/InO_x/NiFe-LDH photoanode reveals a photocurrent density of 5.47 mA cm^{-2} at $1.23 \text{ V}_{\text{RHE}}$ and an ABPE value of 1.19% at $0.795 \text{ V}_{\text{RHE}}$ in 1 M KOH electrolyte, and make it a promising candidate for photoelectrochemical water splitting.

CRediT authorship contribution statement

YG Xia and DR Chen supervised the project. HM Wang performed most of the sample synthesis and characterizations. YG Xia performed all the calculations and wrote this paper. XL Jiao and DR Chen discussed the experimental and theoretical results. N Wen and Z Shu were responsible for some results evaluations. All authors contributed to the overall scientific interpretation and revised this paper.

Declaration of Competing Interest

The authors declare that they have no known competing financial interests or personal relationships that could have appeared to influence the work reported in this paper.

Acknowledgments

This work is financially supported by the Young Scholars Program of Shandong University, the National Natural Science Foundation of China (Grant 21701099), and the Taishan Scholars Climbing Program of Shandong Province (tsdp20150201). The numerical calculations in this Article have been done on the supercomputing system in the Supercomputing Center, Shandong University, Weihai.

Appendix A. Supporting information

Supplementary data associated with this article can be found in the online version at doi:10.1016/j.apcatb.2021.120717.

References

- [1] T. Hisatomi, J. Kubota, K. Domen, Recent advances in semiconductors for photocatalytic and photoelectrochemical water splitting, *Chem. Soc. Rev.* 43 (2014) 7520–7535.
- [2] T. Yao, X. An, H. Han, J.Q. Chen, C. Li, Photoelectrocatalytic materials for solar water splitting, *Adv. Energy Mater.* 8 (2018), 1800210.
- [3] M.R. Nellist, F.A.L. Laskowski, F. Lin, T.J. Mills, S.W. Boettcher, Semiconductor–electrocatalyst interfaces: theory, experiment, and applications in photoelectrochemical water splitting, *Acc. Chem. Res.* 49 (2016) 733–740.
- [4] T.W. Hamann, An adaptive junction, *Nat. Mater.* 13 (2014) 3–4.
- [5] T.J. Mills, F. Lin, S.W. Boettcher, Theory and simulations of electrocatalyst-coated semiconductor electrodes for solar water splitting, *Phys. Rev. Lett.* 112 (2014), 148304.
- [6] J. Li, W. Wan, C.A. Triana, H. Chen, Y. Zhao, C.K. Mavrokefalos, G.R. Patzke, Reaction kinetics and interplay of two different surface states on hematite photoanodes for water oxidation, *Nat. Commun.* 12 (2021) 255.
- [7] F. Lin, B.F. Bachman, S.W. Boettcher, Impact of electrocatalyst activity and ion permeability on water-splitting photoanodes, *J. Phys. Chem. Lett.* 6 (2015) 2427–2433.
- [8] C.-W. Tung, T.-R. Kuo, C.-S. Hsu, Y. Chuang, H.-C. Chen, C.-K. Chang, C.-Y. Chien, Y.-J. Lu, T.-S. Chan, J.-F. Lee, J.-Y. Li, H.M. Chen, Light-induced activation of adaptive junction for efficient solar-driven oxygen evolution: in situ unraveling the interfacial metal–silicon junction, *Adv. Energy Mater.* 9 (2019), 1901308.
- [9] L. Meng, D. Rao, W. Tian, F. Cao, X. Yan, L. Li, Simultaneous manipulation of O-doping and metal vacancy in atomically thin $\text{Zn}_{10}\text{In}_{16}\text{S}_{34}$ nanosheet arrays toward improved photoelectrochemical performance, *Angew. Chem. Int. Ed.* 57 (2018) 16882–16887.
- [10] H. Hajibabaei, A.R. Schon, T.W. Hamann, Interface control of photoelectrochemical water oxidation performance with $\text{Ni}_{1-x}\text{Fe}_x\text{O}_y$ modified hematite photoanodes, *Chem. Mater.* 29 (2017) 6674–6683.
- [11] S.A. Lee, T.H. Lee, C. Kim, M.G. Lee, M.-J. Choi, H. Park, S. Choi, J. Oh, H.W. Jang, Tailored NiO_x/Ni cocatalysts on silicon for highly efficient water splitting photoanodes via pulsed electrodeposition, *ACS Catal.* 8 (2018) 7261–7269.
- [12] S. Zhang, B. Zhang, D. Chen, Z. Guo, M. Ruan, Z. Liu, Promising pyro-photo-electric catalysis in NaNbO_3 via integrating solar and cold-hot alternation energy in pyroelectric-assisted photoelectrochemical system, *Nano Energy* 79 (2021), 105485.
- [13] S. Zhang, Z. Liu, D. Chen, Z. Guo, M. Ruan, Oxygen vacancies engineering in TiO_2 homojunction/ ZnFe-LDH for enhanced photoelectrochemical water oxidation, *Chem. Eng. J.* 395 (2020), 125101.
- [14] D. Chen, Z. Liu, S. Zhang, Enhanced PEC performance of hematite photoanode coupled with bimetallic oxyhydroxide NiFeOOH through a simple electroless method, *Appl. Catal. B* 265 (2020), 118580.
- [15] F. Lin, S.W. Boettcher, Adaptive semiconductor/electrocatalyst junctions in water-splitting photoanodes, *Nat. Mater.* 13 (2014) 81–86.
- [16] X. Ren, C. Wei, Y. Sun, X. Liu, F. Meng, X. Meng, S. Sun, S. Xi, Y. Du, Z. Bi, G. Shang, A.C. Fisher, L. Gu, Z.J. Xu, Constructing an adaptive heterojunction as a highly active catalyst for the oxygen evolution reaction, *Adv. Mater.* 32 (2020), 2001292.
- [17] Y. Li, L. Zhang, X. Xiang, D. Yan, F. Li, Engineering of ZnCo -layered double hydroxide nanowalls toward high-efficiency electrochemical water oxidation, *J. Mater. Chem. A* 2 (2014) 13250–13258.
- [18] B. Klahr, S. Gimenez, F. Fabregat-Santiago, J. Bisquert, T.W. Hamann, Electrochemical and photoelectrochemical investigation of water oxidation with hematite electrodes, *Energy Environ. Sci.* 5 (2012) 7626–7636.
- [19] C. Li, A. Li, Z. Luo, J. Zhang, X. Chang, Z. Huang, T. Wang, J. Gong, Surviving high-temperature calcination: ZrO_2 -induced hematite nanotubes for photoelectrochemical water oxidation, *Angew. Chem. Int. Ed.* 56 (2017) 4150–4155.
- [20] D. Monllor-Satoca, M. Bärtsch, C. Fàbrega, A. Genç, S. Reinhard, T. Andreu, J. Arbiol, M. Niederberger, J.R. Morante, What do you do, titanium? Insight into the role of titanium oxide as a water oxidation promoter in hematite-based photoanodes, *Energy Environ. Sci.* 8 (2015) 3242–3254.
- [21] P. Tang, H. Xie, C. Ros, L. Han, M. Biset-Peiró, Y. He, W. Kramer, A.P. Rodríguez, E. Saucedo, J.R. Galán-Mascarós, T. Andreu, J.R. Morante, J. Arbiol, Enhanced photoelectrochemical water splitting of hematite multilayer nanowire photoanodes by tuning the surface state via bottom-up interfacial engineering, *Energy Environ. Sci.* 10 (2017) 2124–2136.
- [22] R. Yalavarthi, R. Zboril, P. Schmuki, A. Naldoni, Š. Kment, Elucidating the role of surface states of BiVO_4 with Mo doping and a CoOOH co-catalyst for photoelectrochemical water splitting, *J. Power Sources* 483 (2021), 229080.
- [23] H.I. Yeom, J.B. Ko, G. Mun, S.H.K. Park, High mobility polycrystalline indium oxide thin-film transistors by means of plasma-enhanced atomic layer deposition, *J. Mater. Chem. C* 4 (2016) 6873–6880.
- [24] B. Guo, A. Batool, G. Xie, R. Boddula, L. Tian, S.U. Jan, J.R. Gong, Facile integration between Si and catalyst for high-performance photoanodes by a multifunctional bridging layer, *Nano Lett.* 18 (2018) 1516–1521.
- [25] D.K. Zhong, S. Choi, D.R. Gamelin, Near-complete suppression of surface recombination in solar photoelectrolysis by “Co-Pi” catalyst-modified W: BiVO_4 , *J. Am. Chem. Soc.* 133 (2011) 18370–18377.
- [26] R.R. Sawant, K.Y. Rajpure, C.H. Bhosale, Determination of CdIn_2S_4 semiconductor parameters by (photo)electrochemical technique, *Phys. B* 393 (2007) 249–254.
- [27] Z. Li, W. Luo, M. Zhang, J. Feng, Z. Zou, Photoelectrochemical cells for solar hydrogen production: current state of promising photoelectrodes, methods to improve their properties, and outlook, *Energy Environ. Sci.* 6 (2013) 347–370.
- [28] E.A. Ponomarev, L.M. Peter, A generalized theory of intensity-modulated photocurrent spectroscopy (IMPS), *Electroanal. Chem.* 396 (1995) 219–226.
- [29] G. Kresse, J. Hafner, Ab initio molecular dynamics for liquid metals, *Phys. Rev. B* 47 (1993) 558–561.
- [30] G. Kresse, J. Furthmüller, Efficiency of ab-initio total-energy calculations for metals and semiconductors using a plane-wave basis set, *Comp. Mater. Sci.* 6 (1996) 15–50.
- [31] F. Dionigi, Z. Zeng, I. Sinev, T. Merzdorf, S. Deshpande, M.B. Lopez, S. Kunze, I. Zegkinoglou, H. Sarodnik, D. Fan, A. Bergmann, J. Drnec, J. Fd Araujo, M. Gleich, D. Teschner, J. Zhu, W.-X. Li, J. Greeley, B.R. Cuenya, P. Strasser, In-situ structure and catalytic mechanism of NiFe and CoFe layered double hydroxides during oxygen evolution, *Nat. Commun.* 11 (2020) 2522.
- [32] J.M. Yu, J. Lee, Y.S. Kim, J. Song, J. Oh, S.M. Lee, M. Jeong, Y. Kim, J.H. Kwak, S. Cho, C. Yang, J.-W. Jang, High-performance and stable photoelectrochemical water splitting cell with organic-photoactive-layer-based photoanode, *Nat. Commun.* 11 (2020) 5509.
- [33] Y. Huang, Y. Yu, Y. Xin, N. Meng, Y. Yu, B. Zhang, Promoting charge carrier utilization by integrating layered double hydroxide nanosheet arrays with porous BiVO_4 photoanode for efficient photoelectrochemical water splitting, *Sci. China Mater.* 60 (2017) 193–207.
- [34] S. Chen, T. Takata, K. Domen, Particulate photocatalysts for overall water splitting, *Nat. Rev. Mater.* 2 (2017) 17050.
- [35] Z. Luo, B. Liu, H. Li, X. Chang, W. Zhu, T. Wang, J. Gong, Multifunctional nickel film protected n-type silicon photoanode with high photovoltage for efficient and stable oxygen evolution reaction, *Small Methods* 3 (2019), 1900212.
- [36] S. Hu, M.R. Shaner, J.A. Beardslee, M. Lichterman, B.S. Brunschwig, N.S. Lewis, Amorphous TiO_2 coatings stabilize Si, GaAs, and GaP photoanodes for efficient water oxidation, *Science* 344 (2014) 1005.
- [37] S. Oh, S. Jung, Y.H. Lee, J.T. Song, T.H. Kim, D.K. Nandi, S.-H. Kim, J. Oh, Hole-selective $\text{CoO}_x/\text{SiO}_x/\text{Si}$ heterojunctions for photoelectrochemical water splitting, *ACS Catal.* 8 (2018) 9755–9764.
- [38] W. Xu, W. Tian, L. Meng, F. Cao, L. Li, Interfacial chemical bond-modulated Z-scheme charge transfer for efficient photoelectrochemical water splitting, *Adv. Energy Mater.* 11 (2021), 2003500.
- [39] S.-H. Lee, S.W. Lee, T. Oh, S.H. Petrosko, C.A. Mirkin, J.-W. Jang, Direct observation of plasmon-induced interfacial charge separation in metal/semiconductor hybrid nanostructures by measuring surface potentials, *Nano Lett.* 18 (2018) 109–116.
- [40] R. Chen, S. Pang, H. An, T. Dittrich, F. Fan, C. Li, Giant defect-induced effects on nanoscale charge separation in semiconductor photocatalysts, *Nano Lett.* 19 (2019) 426–432.
- [41] B. Klahr, S. Gimenez, F. Fabregat-Santiago, T. Hamann, J. Bisquert, Water oxidation at hematite photoelectrodes: the role of surface states, *J. Am. Chem. Soc.* 134 (2012) 4294–4302.
- [42] H. Wang, Y. Xia, H. Li, X. Wang, Y. Yu, X. Jiao, D. Chen, Highly active deficient ternary sulfide photoanode for photoelectrochemical water splitting, *Nat. Commun.* 11 (2020) 3078.
- [43] F. Fabregat-Santiago, G. Garcia-Belmonte, I. Mora-Seró, J. Bisquert, Characterization of nanostructured hybrid and organic solar cells by impedance spectroscopy, *Phys. Chem. Chem. Phys.* 13 (2011) 9083–9118.
- [44] K. George, T. Khachatryan, M. van Berkel, V. Sinha, A. Bieberle-Hütter, Understanding the impact of different types of surface states on photoelectrochemical water oxidation: a microkinetic modeling approach, *ACS Catal.* 10 (2020) 14649–14660.
- [45] Z. Li, W. Luo, M. Zhang, J. Feng, Z. Zou, Photoelectrochemical cells for solar hydrogen production: current state of promising photoelectrodes, methods to improve their properties, and outlook, *Energy Environ. Sci.* 6 (2013) 347–370.

- [46] Z. Tian, P. Zhang, P. Qin, D. Sun, S. Zhang, X. Guo, W. Zhao, D. Zhao, F. Huang, Novel black $\text{BiVO}_4/\text{TiO}_{2-x}$ photoanode with enhanced photon absorption and charge separation for efficient and stable solar water splitting, *Adv. Energy Mater.* 9 (2019), 1901287.
- [47] S. Feng, T. Wang, B. Liu, C. Hu, L. Li, Z.-J. Zhao, J. Gong, Enriched surface oxygen vacancies of photoanodes by photoetching with enhanced charge separation, *Angew. Chem. Int. Ed.* 59 (2020) 2044–2048.
- [48] C. Zachäus, F.F. Abdi, L.M. Peter, R. van de Krol, Photocurrent of BiVO_4 is limited by surface recombination, not surface catalysis, *Chem. Sci.* 8 (2017) 3712–3719.
- [49] G. Liu, S. Ye, P. Yan, F. Xiong, P. Fu, Z. Wang, Z. Chen, J. Shi, C. Li, Enabling an integrated tantalum nitride photoanode to approach the theoretical photocurrent limit for solar water splitting, *Energy Environ. Sci.* 9 (2016) 1327–1334.
- [50] S. Zhao, Y. Wang, J. Dong, C.-T. He, H. Yin, P. An, K. Zhao, X. Zhang, C. Gao, L. Zhang, J. Lv, J. Wang, J. Zhang, A.M. Khattak, N.A. Khan, Z. Wei, J. Zhang, S. Liu, H. Zhao, Z. Tang, Ultrathin metal-organic framework nanosheets for electrocatalytic oxygen evolution, *Nat. Energy* 1 (2016) 16184.